Double Hidden Layer Output Feedback Neural Adaptive Global Sliding Mode Control of Active Power Filter

Juntao Fei, *Senior Member, IEEE*, and Yundi Chu

***Abstract*—In this paper, a self-regulated double hidden layer output feedback neural network (DHLFNN) is presented to control an active power filter (APF) system as a current controller, which is conducive to the improvement of the response characteristic and power quality. First, a global sliding mode controller is introduced because it is effective in achieving overall robustness during the system response. A new output feedback neural structure that has two hidden layers is proposed to make the parameters adaptively adjust themselves and stabilize to their best values. A higher accuracy and stronger generalization ability can be also obtained by reducing the number of network weights and accelerating the network training speed owing to the strong fitting and presentation ability of two-layer activation functions. Furthermore, the designed feedback loops of the neural network play a significant role in possessing associative memory and rapid system convergence. This proposed double hidden layer output feedback neural based global sliding mode controller is simulated on the model of APF and the results show the excellent static and dynamic properties. Experimental results under three cases and comparisons are provided using a fully digital control system to validate the superior performance of the proposed DHLFNN controller.**

***Index Terms*—Active power filter (APF), double hidden layer output feedback neural network (DHLFNN), global sliding mode control, harmonic compensation, single hidden layer output feedback neural network (SHLFNN).**

I. Introduction

IN THE modern society, the performances of lots of electronic and electrical systems are improved with the development of the power electronics devices; however, the wide-ranging applications of nonlinear loads produce a great deal of harmonics inevitably, which cause the pollution of the electrical power system. At present, the inhibition of harmonics has become a significant way to improve the quality of electric energy [1]–[3]. APF is a new power electronic device that could generate compensation currents into the grid to offset the harmonic currents, which may enormously harm the power system. Active power filters (APF) were developed to mitigate problems of passive filters [4]–[6] to obtain high power quality. APF possesses rapid development and bright prospect in application since APF performs better than the passive filter in its lightweight, fast dynamic response, mildly affected by system impedance, and so on. They were quite effective in compensating harmonics and achieving good performances [7]–[10].

To a great extent, the compensation ability of the APF depends on the control strategies. Thus, it is quite significant for designing an effective control technology to realize expected harmonic suppression performance. As a result, lots of control techniques such as sliding mode controller [11], [12], robust adaptive controller [13], [14], fractional order controller [15], backstepping technique [16], [17], repetitive controller [18], neural network algorithm [19], [20], etc., have been utilized to improve the property of the APFs. Ribeiro *et al*. [13] introduced a robust adaptive control strategy of shunt APFs for power factor correction, harmonic compensation, and balancing of nonlinear loads. A fractional-order repetitive control (RC) strategy at a fixed sampling rate was presented by Zou *et al*. [15] to deal with any periodic signal of variable frequency. A novel concept of quasi-output feedback global sliding mode tracker to achieve robust tracking and model following for uncertain systems was put forward in [17]. A detailed design, analysis, and application of the controller for a shunt APF based on a pulsewidth modulation dc-to-ac voltage source converter were discussed in [18]. Chu *et al*. [20] were concerned with an adaptive dynamic special PID global sliding mode controller with an RBF neural network for a three-phase APF to obtain global robustness.

In practice, there are parameter variations and external disturbances that are difficult to know in APF systems; as a result, global sliding mode control has been employed in controlling nonlinear systems [21]–[23]. Hu *et al*. [21] focused on a global sliding mode controller based on a hyperbolic tangent function with IPF compensation for matrix rectifiers. Mobayen *et al*. [23] presented a novel global sliding mode controller for a class of nonlinear dynamic systems to modify the system robustness. However, as global sliding mode controller is based on a good

Manuscript received November 7, 2018; revised January 3, 2019 and March 27, 2019; accepted June 16, 2019. Date of publication June 25, 2019; date of current version December 13, 2019. This work was supported in part by the National Science Foundation of China under Grant 61873085, in part by the Natural Science Foundation of Jiangsu Province under Grants BK20171198 and BK20170303, in part by The University Graduate Research and Innovation Projects of Jiangsu Province under Grant 2018B676X14, and in part by The Fundamental Research Funds for the Central Universities under Grants 2017B07011, 2017B20014, and 2017B03014. Recommended for publication by Associate Editor L. Dalessandro. *(Corresponding author: Yundi Chu.)*

The authors are with the College of Energy and Electrical Engineering, Hohai University, Nanjing 210098, China, with the Jiangsu Key Laboratory of Power Transmission and Distribution Equipment Technology, China, and also with the College of IoT Engineering, Hohai University, Changzhou 213022, China (e-mail: jtfei@yahoo.com; yundi_chu @yahoo.com).

Color versions of one or more of the figures in this paper are available online at http://ieeexplore.ieee.org.

Digital Object Identifier 10.1109/TPEL.2019.2925154

understanding of a model structure, the scheme cannot be easily implemented to achieve favorable tracking performance in the presence of system uncertainties and external disturbances. The feedforward neural network has been widely applied in identification and control for its strong capacity in approximating to any unknown smooth functions of dynamic systems [24]–[27]. In order to stabilize a class of uncertain nonlinear systems with full-state constraints, an adaptive neural network estimator was investigated in [25]. Bouhoune *et al*. [27] combined neural networks and fuzzy techniques in the form of hybrid control for a three-phase induction machine.

Faced with the poor dynamic property of the feedforward neural network, output feedback neural network (FNN), which is composed of feedforward neural and feedback loops, can acquire more dynamic information. By means of superior nonlinear adaptation and learning ability of FNN, the parameters in FNN can be adjusted simply compared with the conventional NN controller [28]–[32]. For example, a novel output FNN based controller was suggested for a single-phase inverter with an *LCL* filter to approximate to optimal control in [28]. Fei *et al*. [30] studied an adaptive sliding mode control for a class of nonlinear dynamic systems using a double-loop output FNN structure. An adaptive dynamic sliding mode control system with output feedback radial basis function (RBF) network for indirect field-orientation control induction motor drive was proposed by El-Sousy in [32].

It is hard for the normal neural network with a single hidden layer to estimate some quite complex functions with high accuracy in fact. In addition, a shallow network may need a considerable number of neurons, which will lead to a serious problem of computational complexity, long training time, and high memory consumption. While there are far less parameters in the deep network, which can also obtain satisfactory control precision. As a consequence, a deep neural network with multi-layered perceptron is designed to obtain stronger function fitting capacity and high learning accuracy [33]–[36]. It was reported in [33] that an artificial neural network, in the form of a hybrid double hidden layer perceptron, can be used to provide the best prediction performance in the classification of unknown odorants into their respective chemical class. Ahmadi *et al*. [34] developed a novel human iris recognition approach based on a multi-layer perceptron NN in order to increase generalization performance. Makondo *et al*. [35] made an effort to explore the feasibility of using a multilayer perceptron neural network as a test oracle.

Motivated from the above discussion regarding output FNN and multi-layer perceptron neural network, a double hidden layer output feedback neural based adaptive global sliding mode controller is presented for APF with the unpredictable perturbation effect from the parameter variation and external load disturbance to compensate harmonic current and improve power quality. The presented control scheme possesses significant theoretical and practical value for improving total harmonic distortion (THD), strengthening the quality of power supply and promoting the application of APF. The contributions of proposed methods compared with existing works are summarized as follows.

1) An original output FNN with two hidden layers is designed to estimate the uncertainties regardless of unknown system characteristics and external disturbances. In the novel NN, the weights and output signals calculated in the last step are stored and used as the feedback signals in the feedback loop. Since the new structure possesses the advantages of deep learning neural network and output feedback NN, it can make the network be more powerful to learn complex things while the output signal is also captured; thus the new designed double hidden layer neural network with output feedback can achieve better approximation performance compared with the regular NNs without output feedback loop [24]–[27] or the regular FNNs with a single hidden layer [28]–[32]. Moreover, from a practical application point of view, the double hidden layer neural network is a more expressive network than the conventional one with a single hidden layer. The common network of a single hidden layer neural needs more exponentially nodes than deep network such as a double hidden layer neural network to complete approximation. Its core is: the composition of functions is more effective than the linear sum of functions. It is in favor of control precision and enhancement of response speed for dynamic systems.
2) As the hidden layer in the neural network consists of activation functions, which play a significant role in making the network have the strong fitting ability, the neural network with double hidden layers could realize more complex function fitting and higher training precision by fast convergence. Each node and weight has its meaning and represents a special part of the network. Moreover, the recombination of activation functions gives the practical significance of the multi-layered perception neural, which not only can make the network more powerful to learn complex data but also represent the mapping of arbitrary nonlinear function between the input and output.
3) Unlike the general neural network structure, the neurons of the input layer can receive signals, which come back from the neurons of the output layer in the feedback neural structure. It is generally known that neural networks with feedback loops are adept at accepting past memory elements, that is, more information will be transmitted to the output node and the system can achieve better approximation performance and superior dynamic capability compared with the conventional feedforward neural networks (NNs). Furthermore, the six sets of adaptive parameters of two sets of central vectors, two sets of base widths, weight, and feedback gain all adjust themselves to the optimal values adaptively, demonstrating that the system acquires more stable internal state and better approximation feature in contrast with the pure NNs without feedback loops.
4) A global sliding mode controller based on double hidden layer output feedback neural, which has the salient merit of model-free control with great potential, is designed to generate compensation current for APF to improve compensation performance and suppress harmonics as it is

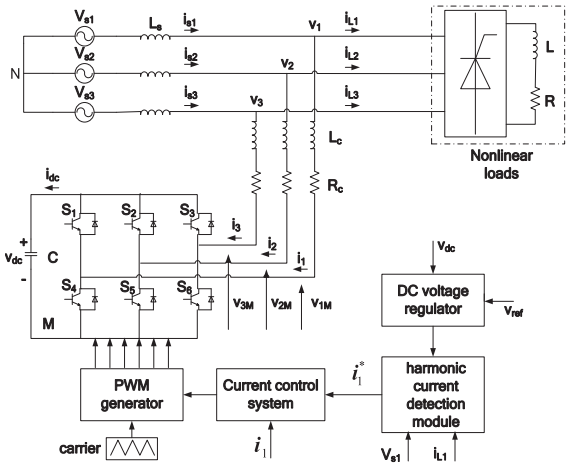

Fig. 1. Block diagram for APF.

difficult to establish an accurate mathematical model for APF systems because of its nonlinearity and uncertainties. The proposed global sliding mode controller can ensure the global robustness especially in the approaching modal status, which also accelerates the response of the system while the conventional sliding mode controller cannot obtain such a feature. The parameters of double hidden layer output feedback neural network (DHLFNN) system regulate themselves online to the optimum stable values and simultaneously adaptive laws can guarantee the Lyapunov stability of the closed-loop system. Even for a complex system, we can also achieve satisfactory performance, which validates the excellent control effect of the presented global sliding mode control using DHLFNN compensator.

This paper is organized as follows. In Section II, the principle of APF is given. Section III explains the structure of DHLFNN, and Section IV investigates the design of DHLFNN-based global sliding mode controller for APF and proves the stabilities of the designed control systems. Section V shows the simulation study for an APF along with several comparisons. Experimental results are provided in Section VI. This paper ends with concluding remarks outlined in Section VII.

II. Principle of APF

Fig. 1 shows the block diagram of three-phase shunt APF. The APF consists of harmonic current detection module, control system, and main circuit. The rapid detection of harmonic current that is based on the instantaneous reactive power theory is most widely used in harmonic current detection module. The control system can be divided into two separate parts, namely the current control system to ensure the accurate tracking of the reference current and the dc voltage regulator to achieve power balance between the dc side and ac side by regulating the dc voltage to its reference value. The main circuit that contains power switching devices generates compensation currents according to the control signal from the control system.

The basic working principle of APF is described as follows. First, detect the harmonic current from the power system and then produce the compensation current, which is equal in the opposite direction of the harmonic current, eliminating harmonic current in the power grid.

In Fig. 1, v_{s1}, v_{s2}, and v_{s3} are the grid voltages, i_{s1}, i_{s2}, and i_{s3} are the power currents, i_{L1}, i_{L2}, and i_{L3} are the load currents, v_1, v_2, and v_3 are the voltages of public join points, i_1, i_2, and i_3 are the compensation current of APF, C is the capacitor of the dc side, $v_{\rm dc}$ is the voltage of *C*, $i_{\rm dc}$ is the current of *C*, L_c is the inductance of the ac side, and R_c is the equivalent resistance.

The dynamic model of APF is given in the following part. The circuit equations are obtained when applying Kirchhoff's rules to this system

$$\begin{cases} v_1 = L_c \frac{di_1}{dt} + R_c i_1 + v_{1M} + v_{MN} \\ v_2 = L_c \dfrac{di_2}{dt} + R_c i_2 + v_{2M} + v_{MN} \\ v_3 = L_c \dfrac{di_3}{dt} + R_c i_3 + v_{3M} + v_{MN} \end{cases} \tag{1}$$

where the parameter of ν_{MN} is the voltage between points *M* and *N*.

Assuming that $v_1 + v_2 + v_3 = 0$, $i_1 + i_2 + i_3 = 0$, we have

$$v_{MN} = -\frac{1}{3} \sum_{m=1}^{3} v_{mM}. \tag{2}$$

The switching function c_k indicates the ON/OFF status of the IGBT bridge, which can be defined as

$$c_k = \begin{cases} 1, & \text{if } S_k \text{ is ON and } S_{k+3} \text{ is OFF} \\ 0, & \text{if } S_k \text{ is OFF and } S_{k+3} \text{ is ON} \end{cases} \tag{3}$$

where $k = 1, 2, 3$.

Taking $v_{kM} = c_k v_{\rm dc}$ into account, and (1) becomes

$$\begin{cases} \dfrac{di_1}{dt} = -\dfrac{R_c}{L_c} i_1 + \dfrac{v_1}{L_c} - \dfrac{v_{\rm dc}}{L_c} \left(c_1 - \dfrac{1}{3} \sum\limits_{m=1}^{3} c_m \right) \\ \dfrac{di_2}{dt} = -\dfrac{R_c}{L_c} i_2 + \dfrac{v_2}{L_c} - \dfrac{v_{\rm dc}}{L_c} \left(c_2 - \dfrac{1}{3} \sum\limits_{m=1}^{3} c_m \right) \\ \dfrac{di_3}{dt} = -\dfrac{R_c}{L_c} i_3 + \dfrac{v_3}{L_c} - \dfrac{v_{\rm dc}}{L_c} \left(c_3 - \dfrac{1}{3} \sum\limits_{m=1}^{3} c_m \right). \end{cases} \tag{4}$$

Then d_{nk} is defined, called the switching state function as

$$d_{nk} = \left(c_k - \frac{1}{3} \sum_{m=1}^{3} c_m \right)_n. \tag{5}$$

Assume unknown external disturbance and parameter variation as $Q = [q_1 \quad q_2 \quad q_3]^T$, we have

$$\begin{cases} \dfrac{di_1}{dt} = -\dfrac{R_{c1}}{L_{c1}} i_1 + \dfrac{v_1}{L_{c1}} - \dfrac{v_{\rm dc}}{L_{c1}} d_{n1} + q_1 \\ \dfrac{di_2}{dt} = -\dfrac{R_{c1}}{L_{c1}} i_2 + \dfrac{v_2}{L_{c1}} - \dfrac{v_{\rm dc}}{L_{c1}} d_{n2} + q_2 \\ \dfrac{di_3}{dt} = -\dfrac{R_{c1}}{L_{c1}} i_3 + \dfrac{v_3}{L_{c1}} - \dfrac{v_{\rm dc}}{L_{c1}} d_{n3} + q_3. \end{cases} \tag{6}$$

The derivative of (6) is

$$\begin{cases} \ddot{i}_1 = \dfrac{R_{c1}^2}{L_{c1}^2} i_1 + \dfrac{\dot{v}_1}{L_{c1}} - \dfrac{R_{c1} v_1}{L_{c1}^2} + \dfrac{R_{c1} v_{\rm dc}}{L_{c1}^2} d_{n1} - \dfrac{v_{dc}}{L_{c1}} \dot{d}_{n1} \\ \qquad + \dot{q}_1 - \dfrac{R_{c1}}{L_{c1}} q_1 \\ \ddot{i}_2 = \dfrac{R_{c1}^2}{L_{c1}^2} i_2 + \dfrac{\dot{v}_2}{L_{c1}} - \dfrac{R_{c1} v_2}{L_{c1}^2} + \dfrac{R_{c1} v_{\rm dc}}{L_{c1}^2} d_{n2} - \dfrac{v_{dc}}{L_{c1}} \dot{d}_{n2} \\ \qquad + \dot{q}_2 - \dfrac{R_{c1}}{L_{c1}} q_2 \\ \ddot{i}_3 = \dfrac{R_{c1}^2}{L_{c1}^2} i_3 + \dfrac{\dot{v}_3}{L_{c1}} - \dfrac{R_{c1} v_3}{L_{c1}^2} + \dfrac{R_{c1} v_{\rm dc}}{L_{c1}^2} d_{n3} - \dfrac{v_{dc}}{L_{c1}} \dot{d}_{n1} \\ \qquad + \dot{q}_3 - \dfrac{R_{c1}}{L_{c1}} q_3 \end{cases}. \tag{7}$$

As we can see, although this is a multiple input multiple output system, there is no mutual coupling among the three phases of "1," "2," and "3." We can transfer this multivariable control into three single variable controls in the design of the current control system. Furthermore, it can be simplified as a problem of single variable control in the case of the symmetrical parameters.

For the sake of simplicity, it is expressed as the following form:

$$\ddot{x} = f(x) + Bu + h_k \tag{8}$$

where x represents i_1, i_2, or i_3, $f(x)$ represents $\frac{R_{c1}^2}{L_{c1}^2} i_1 + \frac{\dot{v}_1}{L_{c1}} - \frac{R_{c1} v_1}{L_{c1}^2}$, $\frac{R_{c1}^2}{L_{c1}^2} i_2 + \frac{\dot{v}_2}{L_{c1}} - \frac{R_{c1} v_2}{L_{c1}^2}$, or $\frac{R_{c1}^2}{L_{c1}^2} i_3 + \frac{\dot{v}_3}{L_{c1}} - \frac{R_{c1} v_3}{L_{c1}^2}$, B represents $\frac{R_{c1} v_{\rm dc}}{L_{c1}^2}$, $\frac{R_{c1} v_{\rm dc}}{L_{c1}^2}$, or $\frac{R_{c1} v_{\rm dc}}{L_{c1}^2}$, h_k represents $-\frac{v_{\rm dc}}{L_{c1}} \dot{d}_{n1} + \dot{q}_1 - \frac{R_{c1}}{L_{c1}} q_1$, $-\frac{v_{\rm dc}}{L_{c1}} \dot{d}_{n2} + \dot{q}_2 - \frac{R_{c1}}{L_{c1}} q_2$, or $-\frac{v_{\rm dc}}{L_{c1}} \dot{d}_{n3} + \dot{q}_3 - \frac{R_{c1}}{L_{c1}} q_3$. The upper bound of the unknown lump uncertainty is given as $\|h_k\| \le H, k = 1, 2, 3$, where H is a positive constant.

III. Structure of DHLFNN

The DHLFNN constructed by a multilayer perceptron has two hidden layers and a dynamic output feedback connection which stands for memory elements. Each node and weight has its meaning and represents a special part in the network. The adaptive parameter learning and structure learning of this new dynamic double hidden layer neural network make the responses of algorithm faster and more accurate than the conventional ones.

As is shown in Fig. 2, the double hidden layer output feedback neural is a four-layer network embedded two hidden perceptrons and an outer feedback connection. The first layer is the input layer, which is composed of signal receiving nodes.

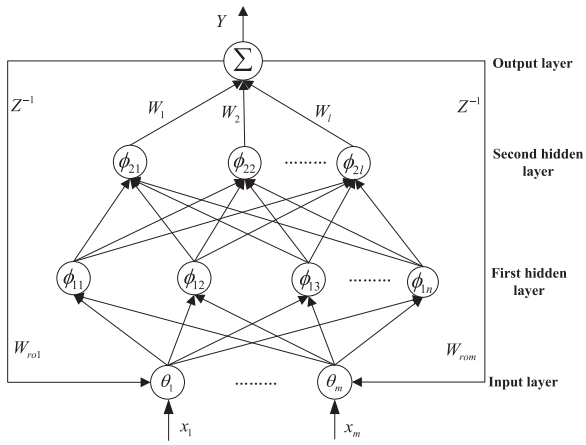

Fig. 2. Structure of DHLFNN.

However, unlike the general neural network structure, the neurons of the input layer can receive signals, which come back from the neurons of the output layer in the neural structure. The second layer is the first hidden layer where neurons in this layer are mainly to complete the calculation of the activation functions. The second hidden layer ulteriorly calculates the Gaussian functions. Furthermore, the recombination of activation functions not only can make the network more powerful to learn complex data but also represent the mapping of arbitrary complex nonlinear function between the input and output. The fourth layer is the output layer, which completes the output calculation of the novel neural network for different inputs. To give a clearer understanding of DHLFNN, the functional structure of each layer will be depicted as follows.

The four layers are the input layer, the first hidden layer, the second hidden layer, and the output layer respectively.

A) First Layer: Input Layer

The input layer of the DHLFNN completes the transmission of the input signal $(X = [x_1 x_2 .. x_m]^T)$ and receives the output signal (exY) of the previous step from the output layer. The output layer is connected to the input layer by the outer weight $W_{ro} = [W_{ro1}, W_{ro2} .. W_{rom}]$ of the novel neural network. The output signal of the input layer is $\theta = [\theta_1, \theta_2 .. \theta_m]^T$, where

$$\theta_i = x_i \cdot W_{\rm roi} \cdot exY, i = 1, 2, \ldots, m. \tag{9}$$

B) Second Layer: The First Hidden Layer

This layer mainly maps the signals from the input space to a higher dimensional hidden space where the signal features are linearly separable and complete calculations of the Gaussian functions. Gaussian functions are introduced to the nodes in the first hidden layer as $\Phi_1 = [\phi_{11}, \phi_{12}, \ldots, \phi_{1n}]^T$, and the Gaussian function of the jth node is expressed as follows:

$$\phi_{1j} = e^{-{\rm net}_{1j}}, \quad {\rm net}_{1j} = \sum_{i=1}^{m} \frac{\|\theta_i - c_{1j}\|^2}{b_{1j}^2}, \quad j = 1, 2, \ldots, n \tag{10}$$

where the central vector is $c_1 = [c_{11}\ c_{12} \dots c_{1n}]^T$ and the base width is $b_1 = [b_{11}\ b_{12} \dots b_{1n}]^T$.

C) Third Layer: The Second Hidden Layer

The signals are mapped from the first hidden layer to this second hidden space, then the Gaussian functions are calculated again. As is similar to the second layer, each node in this layer represents a Gaussian function ϕ_{2k}, which can be expressed in (11) and the total Gaussian function can be denoted as $\Phi_2 = [\phi_{21}, \phi_{22}, \dots, \phi_{2l}]^T$

$$\phi_{2k} = e^{-\mathrm{net}_{2k}}, \quad \mathrm{net}_{2k} = \sum_{i=1}^{n} \frac{\|\phi_{1j} - c_{2k}\|^2}{b_{2k}^2}, \quad k = 1, 2, \dots, l \tag{11}$$

where the central vector is $c_2 = [c_{21}\ c_{22} \dots c_{2l}]^T$, and the base width is $b_2 = [b_{21}\ b_{22} \dots b_{2l}]^T$.

D) Fourth Layer: Output Layer

Neuron in the output layer connects with each neuron in the second hidden layer via the weights $W = [W_1, W_2, \dots, W_l]^T$ and the signal node of the output layer is marked as the sum of all input signals. The signal node of the output layer is marked as $\sum$, which represents the sum of all input signals. It can be written as

$$Y = W \cdot \Phi_2 = W_1\phi_{21} + W_2\phi_{22} + \cdots + W_l\phi_{2l}. \tag{12}$$

The output layer neuron is connected to the input layer neurons by the outer feedback weight value W_{ro}, and the feedback signal is recorded as exY.

IV. DHLFNN-Based Global Sliding Mode Controller for an APF

The current tracking control problem of the APF system is to find a controller so that the current trajectory x can track a reference current trajectory y_d asymptotically. Assuming that all the system parameters are well known, the design of an ideal sliding mode controller for APF systems is described in the following part.

The tracking error is defined as

$$e = x - y_d. \tag{13}$$

Then the derivative of e becomes

$$\dot{e} = \dot{x} - \dot{y}_d. \tag{14}$$

Design the global sliding surface as

$$S = \dot{e} + Ce - f_0(t) \tag{15}$$

where C is a positive matrix, $f_0(t)$ is a function that is specially designed for reaching the global sliding surface, satisfying the following three conditions:

1) $f_0(0) = \dot{e}_0 + Ce_0$;
2) if $t \to \infty$, $f_0(t) \to 0$;
3) $f_0(t)$ has a first derivative.

where e_0 is an initial value of the tracking error.

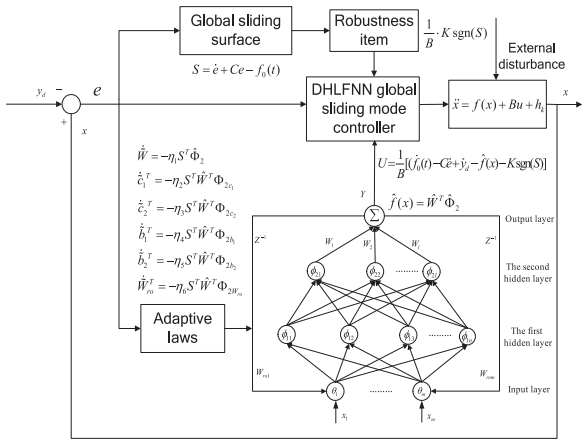

Fig. 3. Block diagram of the global sliding mode controller using DHLFNN.

Hence we can design $f_0(t)$ as

$$f_0(t) = f_0(0)\mathrm{e}^{-k_0 t} \tag{16}$$

where k_0 is a positive constant.

The time derivative of the global sliding surface $\dot{S}$ is

$$\begin{aligned} \dot{S} &= \ddot{e} + C\dot{e} - \dot{f}_0(t) \\ &= \ddot{x} - \ddot{y}_d + C\dot{e} - \dot{f}_0(t) \\ &= f(x) + Bu + h_k - \ddot{y}_d + C\dot{e} - \dot{f}_0(t). \end{aligned} \tag{17}$$

We make $\dot{S} = 0$ to get the equivalent controller

$$u_{\mathrm{eq}} = \frac{1}{B}[\dot{f}_0(t) + \ddot{y}_d - C\dot{e} - f(x) - h_k]. \tag{18}$$

Based on the equivalent controller, a new controller U_{qs} is designed as

$$U_{qs} = \frac{1}{B}[\dot{f}_0(t) + \ddot{y}_d - C\dot{e} - f(x) - K\,\mathrm{sgn}\,(S)] \tag{19}$$

where $u_{\mathrm{sw}} = \frac{1}{B} \cdot K\,\mathrm{sgn}\,(S)$ is a switching controller in which the global sliding mode gain K is a designed positive constant.

Although the designed controller in (19) can guarantee the stability of the system, the controller force could not be carried out due to the unknown part $f(x)$. Considering the strong ability and high precision of approaching any complex function of this designed DHLFNN, it is advisable to use the estimation value of DHLFNN for controller design as shown in Fig. 3.

Assumption 1: There exist optimal weight W^*, center vectors ${c_1}^*$, ${c_2}^*$, standard deviations ${b_1}^*$, ${b_2}^*$, and outer feedback gain W_{ro}^* in approximating to the unknown function $f(x)$, which can be expressed as $f(x) = {W^*}^T {\Phi_2}^* + \varepsilon$, where $\Phi_2^* = \Phi_2^*(X,\ c_1^*,\ c_2^*,\ b_1^*,\ b_1^*,\ W_{ro}^*)$, ε is the mapping error that is uniformly bounded as $\|\varepsilon\| \le \varepsilon_b$, where ε_b is a positive arbitrary small constant.

The output of the DHLFNN for the estimation of unknown function is

$$\hat{f}(x) = \hat{W}^T \hat{\Phi}_2 \tag{20}$$

where $\hat{W}$ is the real estimated weight vector, which is updated online all the time, and $\hat{\Phi}_2$ is the actual estimated value of the six parameters in the DHLFNN structure expressed as $\hat{\Phi}_2 = \hat{\Phi}_2(X, \hat{c}_1, \hat{c}_2, \hat{b}_1, \hat{b}_2, \hat{W}_{ro})$.

Then the error between the real value and the estimation of the unknown function is

$$\begin{aligned} f(x) - \hat{f}(x) &= W^{*T}\Phi_2{}^* - \hat{W}^T\hat{\Phi}_2 + \varepsilon \\ &= W^{*T}(\hat{\Phi}_2 + \tilde{\Phi}_2) - \hat{W}^T\hat{\Phi}_2 + \varepsilon \\ &= W^{*T}\hat{\Phi}_2 + W^{*T}\tilde{\Phi}_2 - \hat{W}^T\hat{\Phi}_2 + \varepsilon \\ &= \tilde{W}^T\hat{\Phi}_2 + \hat{W}^T\tilde{\Phi}_2 + \tilde{W}^T\tilde{\Phi}_2 + \varepsilon \end{aligned} \tag{21}$$

where $\tilde{W}^T\tilde{\Phi}_2 + \varepsilon = \varepsilon_0$ is the approximation error.

The Taylor expansion linearization technique is employed to transform the nonlinear activation function into a partially linear form and $\tilde{\Phi}_2$ can be expressed as

$$\begin{aligned} \tilde{\Phi}_2 &= \frac{\partial\Phi_2}{\partial c_1}|_{c_1=\hat{c}_1}\ ({c_1}^* - \hat{c}_1) + \frac{\partial\Phi_2}{\partial c_2}|_{c_2=\hat{c}_2}\ ({c_2}^* - \hat{c}_2) \\ &\quad + \frac{\partial\Phi_2}{\partial b_1}\Big|_{b_1=\hat{b}_1}\ ({b_1}^* - \hat{b}_1) + \frac{\partial\Phi_2}{\partial b_2}\Big|_{b_2=\hat{b}_2}\ ({b_2}^* - \hat{b}_2) \\ &\quad + \frac{\partial\Phi_2}{\partial W_{ro}}\Big|_{W_{ro}=\hat{W}_{ro}}\ (W_{ro}^* - \hat{W}_{ro}) + O_h \\ &= \Phi_{2c_1}\cdot\tilde{c}_1 + \Phi_{2c_2}\cdot\tilde{c}_2 + \Phi_{2b_1}\cdot\tilde{b}_1 + \Phi_{2b_2}\cdot\tilde{b}_2 \\ &\quad + \Phi_{2W_{ro}}\cdot\tilde{W}_{ro} + O_h \end{aligned} \tag{22}$$

where O_h is a high-order term, Φ_{2c_1}, Φ_{2c_2}, Φ_{2b_1}, Φ_{2b_2}, $\Phi_{2W_{ro}}$ can be expressed in the following forms:

$$\Phi_{2c_1} = \left[\frac{\partial\Phi_{21}}{\partial c_1}\ \ \frac{\partial\Phi_{22}}{\partial c_1}\cdots\frac{\partial\Phi_{2l}}{\partial c_1}\right]^T|_{c_1=\hat{c}_1}$$

$$\Phi_{2c_2} = \left[\frac{\partial\Phi_{21}}{\partial c_2}\ \ \frac{\partial\Phi_{22}}{\partial c_2}\cdots\frac{\partial\Phi_{2l}}{\partial c_2}\right]^T|_{c_2=\hat{c}_2}$$

$$\Phi_{2b_1} = \left[\frac{\partial\Phi_{21}}{\partial b_1}\ \ \frac{\partial\Phi_{22}}{\partial b_1}\cdots\frac{\partial\Phi_{2l}}{\partial b_1}\right]^T\Big|_{b_1=\hat{b}_1}$$

$$\Phi_{2b_2} = \left[\frac{\partial\Phi_{21}}{\partial b_2}\ \ \frac{\partial\Phi_{22}}{\partial b_2}\cdots\frac{\partial\Phi_{2l}}{\partial b_2}\right]^T\Big|_{b_2=\hat{b}_2}$$

$$\Phi_{2W_{ro}} = \left[\frac{\partial\Phi_{21}}{\partial W_{ro}}\ \ \frac{\partial\Phi_{22}}{\partial W_{ro}}\cdots\frac{\partial\Phi_{2l}}{\partial W_{ro}}\right]^T\Big|_{W_{ro}=\hat{W}_{ro}}.$$

Then, the designed controller (19) becomes

$$U = \frac{1}{B}[(\dot{f}_0(t) - C\dot{e} + \ddot{y}_d - \hat{f}(x) - K\,sgn\,(S)]. \tag{23}$$

Consider a Lyapunov function candidate as

$$\begin{aligned} V &= \frac{1}{2}S^TS + \frac{1}{2\eta_1}tr(\tilde{W}^T\tilde{W}) + \frac{1}{2\eta_2}tr(\tilde{c}_1^T\tilde{c}_1) + \frac{1}{2\eta_3}tr(\tilde{c}_2^T\tilde{c}_2) \\ &\quad + \frac{1}{2\eta_4}tr(\tilde{b}_1^T\tilde{b}_1) + \frac{1}{2\eta_5}tr(\tilde{b}_2^T\tilde{b}_2) + \frac{1}{2\eta_6}tr(\tilde{W}_{ro}^T\tilde{W}_{ro}). \end{aligned} \tag{24}$$

Denote

$$\begin{aligned} &\frac{1}{2\eta_1}tr(\tilde{W}^T\tilde{W}) + \frac{1}{2\eta_2}tr(\tilde{c}_1^T\tilde{c}_1) + \frac{1}{2\eta_3}tr(\tilde{c}_2^T\tilde{c}_2) \\ &\quad + \frac{1}{2\eta_4}tr(\tilde{b}_1^T\tilde{b}_1) + \frac{1}{2\eta_5}tr(\tilde{b}_2^T\tilde{b}_2) + \frac{1}{2\eta_6}tr(\tilde{W}_{ro}^T\tilde{W}_{ro}) \end{aligned}$$

as F for simplicity.

Taking the derivative of V and then substituting the control force (23) into it gives

$$\begin{aligned} \dot{V} &= S^T\dot{S} + \dot{F} \\ &= S^T[f(x) + BU + h_k - \ddot{y}_d + C\dot{e} - \dot{f}_0(t)] + \dot{F} \\ &= S^T[f(x) - \hat{f}(x) + h_k - K\,\mathrm{sgn}\,(S)] + \dot{F} \\ &= S^T[W^{*T}\Phi_2{}^* + \varepsilon - \hat{W}^T\hat{\Phi}_2 + h_k - K\,\mathrm{sgn}\,(S)] + \dot{F} \\ &= S^T[\tilde{W}^T\hat{\Phi}_2 + \hat{W}^T\tilde{\Phi}_2 + \varepsilon_0 + h_k - K\,\mathrm{sgn}\,(S)] + \dot{F}. \end{aligned} \tag{25}$$

Then on substituting the Taylor expansion (22) into (25), it can be obtained that

$$\begin{aligned} \dot{V} &= S^T\tilde{W}^T\hat{\Phi}_2 + S^T\hat{W}^T(\Phi_{2c_1}\tilde{c}_1 + \Phi_{2c_2}\cdot\tilde{c}_2 + \Phi_{2b_1}\tilde{b}_1 \\ &\quad + \Phi_{2b_2}\tilde{b}_2 + \Phi_{2W_{ro}}\cdot\tilde{W}_{ro} + O_h) \\ &\quad + S^T[\varepsilon_0 + h_k - K\,\mathrm{sgn}\,(S)] + \frac{1}{\eta_1}tr(\tilde{W}^T\dot{\tilde{W}}) \\ &\quad + \frac{1}{\eta_2}tr(\dot{\tilde{c}}_1{}^T\tilde{c}_1) + \frac{1}{\eta_3}tr(\dot{\tilde{c}}_2{}^T\tilde{c}_2) + \frac{1}{\eta_4}tr(\dot{\tilde{b}}_1{}^T\tilde{b}_1) \\ &\quad + \frac{1}{\eta_5}tr(\dot{\tilde{b}}_2{}^T\tilde{b}_2) + \frac{1}{\eta_6}tr(\dot{\tilde{W}}_{ro}^T\tilde{W}_{ro}). \end{aligned} \tag{26}$$

Setting $S^T\tilde{W}^T\hat{\Phi}_2 + \frac{1}{\eta_1}tr(\tilde{W}^T\dot{\tilde{W}}) = 0$ yields

$$\dot{\tilde{W}} = -\eta_1 S^T\hat{\Phi}_2. \tag{27}$$

Setting $S^T\hat{W}^T\Phi_{2c_1}\tilde{c}_1 + \frac{1}{\eta_2}tr(\dot{\tilde{c}}_1{}^T\tilde{c}_1) = 0$ yields

$$\dot{\tilde{c}}_1{}^T = -\eta_2 S^T\hat{W}^T\Phi_{2c_1}. \tag{28}$$

Setting $S^T\hat{W}^T\Phi_{2c_2}\tilde{c}_2 + \frac{1}{\eta_3}tr(\dot{\tilde{c}}_2{}^T\tilde{c}_2) = 0$ yields

$$\dot{\tilde{c}}_2{}^T = -\eta_3 S^T\hat{W}^T\Phi_{2c_2}. \tag{29}$$

Setting $S^T\hat{W}^T\Phi_{2b_1}\tilde{b}_1 + \frac{1}{\eta_4}tr(\dot{\tilde{b}}_1{}^T\tilde{b}_1) = 0$ yields

$$\dot{\tilde{b}}_1{}^T = -\eta_4 S^T\hat{W}^T\Phi_{2b_1}. \tag{30}$$

Setting $S^T\hat{W}^T\Phi_{2b_2}\tilde{b}_2 + \frac{1}{\eta_5}tr(\dot{\tilde{b}}_2{}^T\tilde{b}_2) = 0$ yields

$$\dot{\tilde{b}}_2{}^T = -\eta_5 S^T\hat{W}^T\Phi_{2b_2}. \tag{31}$$

Setting $S^T\hat{W}^T\Phi_{2W_{ro}}\tilde{W}_{ro} + \frac{1}{\eta_6}tr(\dot{\tilde{W}}_{ro}^T\tilde{W}_{ro}) = 0$ yields

$$\dot{\tilde{W}}_{ro}^T = -\eta_6 S^T\hat{W}^T\Phi_{2W_{ro}}. \tag{32}$$

TABLE I
SYSTEM PARAMETERS FOR SIMULATION

Supply voltage and frequency	$V_{s1}=V_{s2}=V_{s3}=220V, f=50Hz$
Three-phase diode rectifiers parameters	$R=5\Omega$, $L=10mH$
Single-phase diode rectifiers parameters	$R=40\Omega$, $L=10mH$
Active power filter parameters	$L_c=10mH$, $R_c=0.1\Omega$, $C=100\mu F$, $v_{dcref}=700V$
Switching frequency	$f_{sw}=20KHz$

Assume ε_0, O_h are uniformly bounded as $\|\varepsilon_0\| \le \varepsilon_E$, $\|O_h\| \le O_E$. Substituting the adaptive laws in (27)–(32) into (26) leads to

$$\begin{aligned}\dot{V} &= S^T[h_k+\varepsilon_0+O_h-K\,\mathrm{sgn}\,(S)]\\ &= S^T(h_k+\varepsilon_0+O_h)-K\|S\|\\ &\le \|S\|\,\|h_k+\varepsilon_0+O_h\|-K\|S\|\\ &\le \|S\|\,(H+\varepsilon_E+O_E-K). \end{aligned} \tag{33}$$

The following inequality is true if $K > H+\varepsilon_E+O_E$, then $\dot{V}<0$. The negative definite of $\dot{V}$ ensures that V, S are all bounded. It can be concluded that $\dot{S}$ is also bounded. The inequality $\dot{V} \le \|S\|(H+\varepsilon_E+O_E-K)$ implies that S is integrable as $\int_0^t \|S\|dt \le \frac{1}{H+\varepsilon_E+O_E-K}[V(t)-V(0)]$. Since $V(0)$ is bounded and $V(t)$ is nonincreasing and bounded, it can be concluded that $\lim_{t\to\infty}\int_0^t \|S\|dt$ is bounded. Since $\lim_{t\to\infty}\int_0^t \|S\|dt$ is bounded and $\dot{S}$ is also bounded, according to Barbalat's lemma, $S(t)$ will asymptotically converge to zero, $\lim_{t\to\infty} S(t)=0$. Thus the designed DHLFNN controller can guarantee the asymptotic stability of the closed-loop system.

V. SIMULATION STUDY

To verify the performance of the designed novel strategy of adaptive double hidden layer output feedback neural global sliding mode controller for APF, detailed simulation studies are implemented using MATLAB/Simulink package with SimPower Toolbox. The system parameters utilized in the simulation are collected in Table I. The effectiveness of the proposed method can be demonstrated from the following steady-state responses and comparisons for harmonic compensation.

In the global sliding mode controller, we choose the following parameters as $C=\mathrm{diag}\{1300,1300,1300\}$, $K=500$, $k_0=100$. In the adaptive double hidden layer output feedback neural controller, the parameters are selected as $\eta_1=0.012$, $\eta_2=0.12$, $\eta_3=0.1$, $\eta_4=0.1$, $\eta_5=0.01$, $\eta_6=0.2$. The initial values of the center vectors and width vectors of Gaussian function are $c_1=[-3\ -1.5\ 0\ 1.5\ 3]^T$, $b_1=[1\ 1\ 1\ 1\ 1]^T$, $c_2=[-3\ -1.5\ 0\ 1.5\ 3]^T$, $b_2=[1\ 1\ 1\ 1\ 1]^T$. The initial weights are set to random numbers between -1 and 1.

When $t=0.04$ s, the switch of compensation circuit is closed and APF begins to work. The source current is equal to the load current when the APF is not connected, and dc capacitor voltage is 0.

A. Steady-State Response for Harmonic Compensation

Fig. 4 shows the curve of load current i_L, the curve of source current i_s, the tracking trajectory of compensation current i_c, and the tracking error of compensation current (select one phase current to analyze) in (a)–(d), respectively. From the load current in Fig. 4(a), it is apparent that distortion is very serious, which is greatly harmful to the power grid. Source current in Fig. 4(b) is well compensated after applying APF with the proposed controller into the grid at the time of 0.04 s to purify harmonic pollution effectively, where it is almost close to a smooth and sinusoidal wave. Moreover, the tracking trajectory and tracking error of the compensation current can be observed in Fig. 4(c) and (d), where both the tracking performance and the tracking error are in a good state, indicating the good stability and robustness.

THD using the designed novel double hidden layer output feedback neural based global sliding mode control is depicted in Fig. 5(b). THD at 0.06 s is 1.82% after APF is applied to work, whereas the one without APF is relatively extremely high (24.72%) in Fig. 5(b). From the simulation results above, it is clear that the proposed advanced controller is quite efficient to control the APF system with respect to the occurrence of external disturbances and parameter uncertainties.

Figs. 6–11 display the adaptive adjustment curves of the six sets of parameters in DHLFNN. All these parameters of two base widths b_1, b_2, two center vectors c_1, c_2, the network weight W, and the feedback gain W_{ro} are updated online by the adaptive laws and tuned in the Lyapunov sense transitorily to be stable to their optimal values. It is shown that system responses can achieve the satisfactory results, demonstrating the strong robustness and superior self-adjusting ability of the novel designed DHLFNN controller.

To verify the outstanding property of the proposed new controller more convincingly, we make a comparative study. Figs. 12 and 13 are the comparisons of tracking trajectories and tracking errors of the compensation currents using DHLFNN and single hidden layer output feedback neural network (SHLFNN), respectively. As can be seen from the plots, the strategy of the DHLFNN (red dashed line) has smoother tracking performance and smaller tracking error than the SHLFNN (blue point line). Furthermore, the inner state of the whole system is more stable and has less dramatic changes by the DHLFNN. Fig. 14 shows the spectrum analysis of the SHLFNN, compared to the DHLFNN, THD under the SHLFNN (2.06%) is a little higher

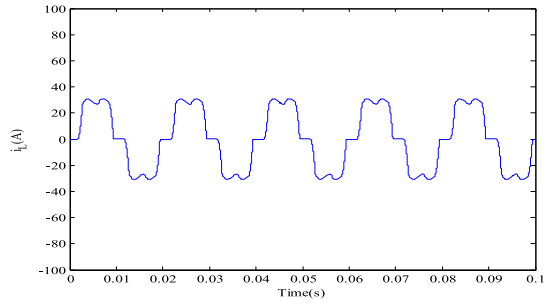

(a)

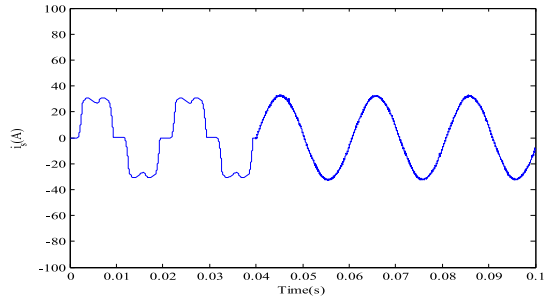

(b)

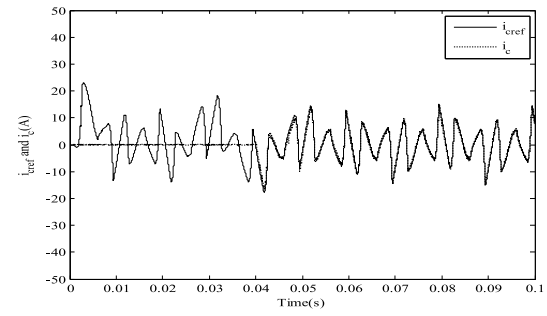

(c)

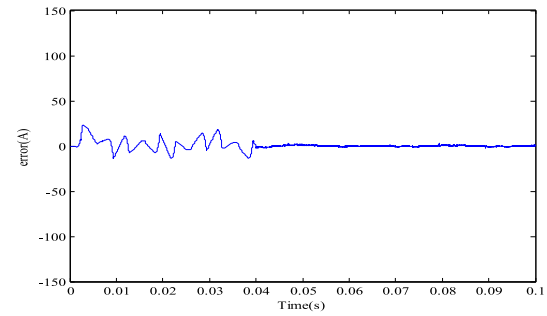

(d)

Fig. 4. Steady-state responses using the proposed controller. (a) The curve of load current. (b) The curve of source current. (c) The tracking trajectory of compensation current. (d) The tracking error of compensation current.

than the one in Fig. 5(b) which indicates the good ability to eliminate harmonics of the DHLFNN structure. It is concluded that the double hidden layer output feedback network has stronger function fitting ability, higher approximation precision, and generalization ability than the SHLFNN.

Fig. 15 draws the dc-link voltage of the APF in the simulation, from which it can be seen that when the load changes at 0.1 s, the

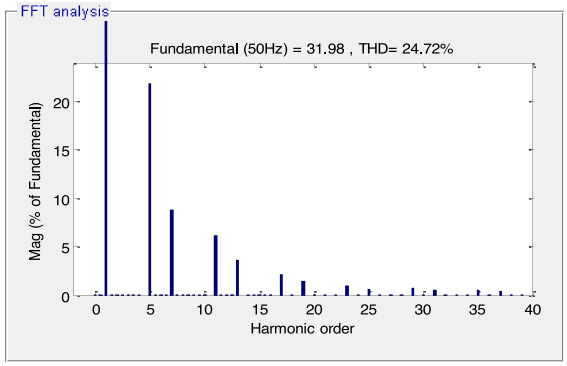

(a)

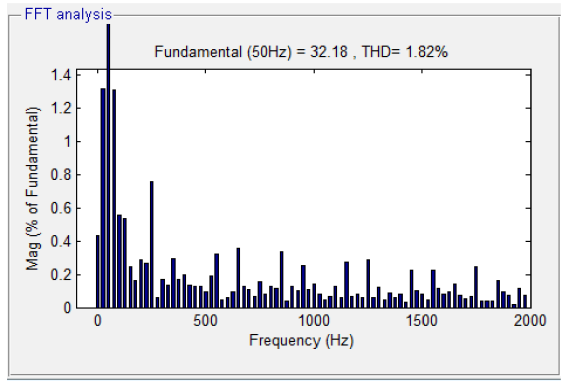

(b)

Fig. 5. The analysis of the harmonic spectrum of DHLRNN. (a) THD before compensation by APF. (b) THD after compensation by APF.

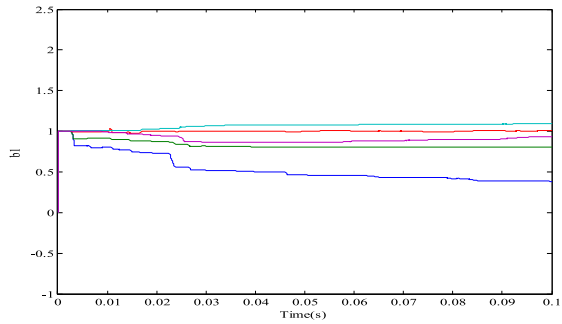

Fig. 6. Adaptation of the width b_1 of DHLFNN.

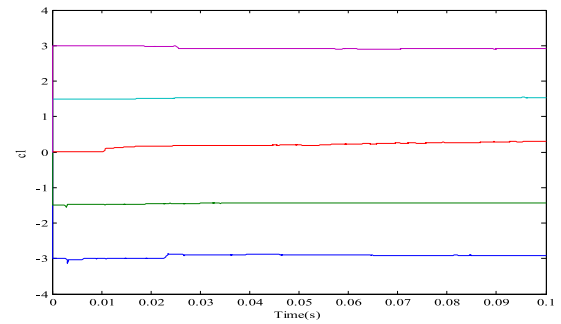

Fig. 7. Adaptation of the center c_1 of DHLFNN.

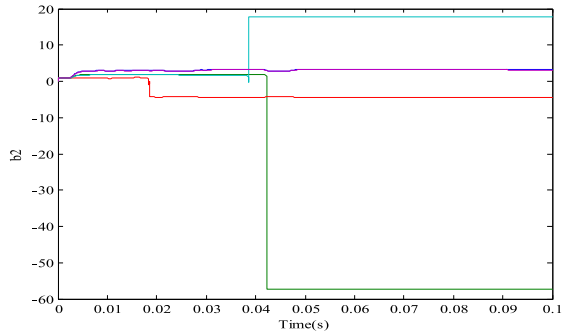

Fig. 8. Adaptation of the width b_2 of DHLFNN.

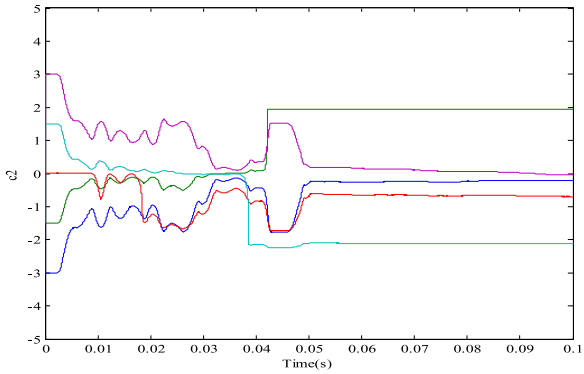

Fig. 9. Adaptation of the center c_2 of DHLFNN.

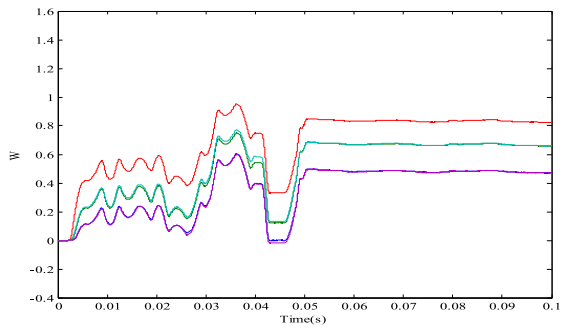

Fig. 10. Adaptation of the weight W of DHLFNN.

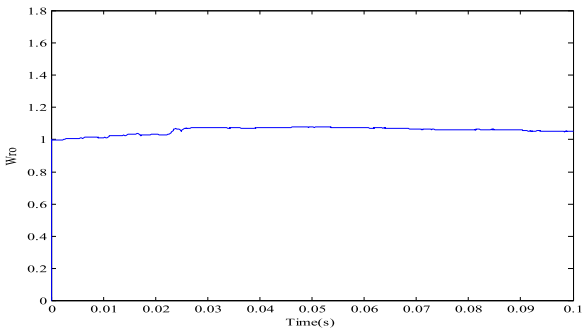

Fig. 11. Adaptation of the outer feedback W_{ro} of DHLFNN.

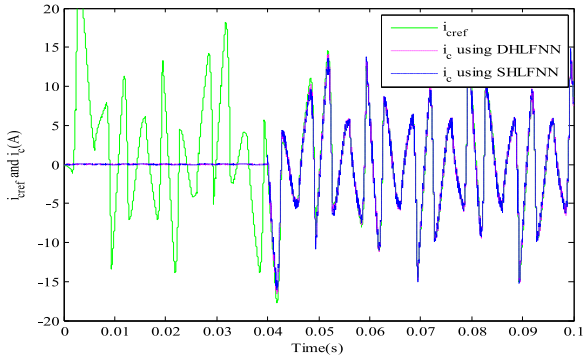

Fig. 12. Tracking trajectories comparison of compensation currents (DHLFNN-SHLFNN).

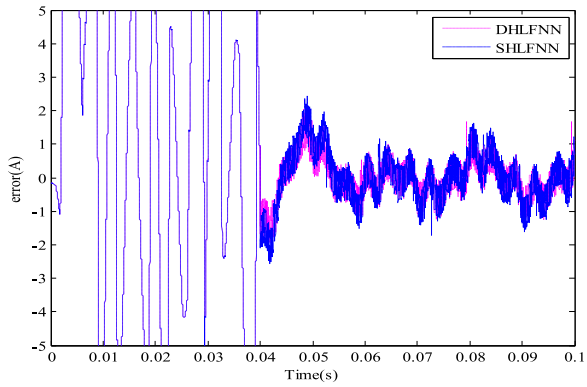

Fig. 13. Tracking errors comparison of compensation currents (DHLFNN-SHLFNN).

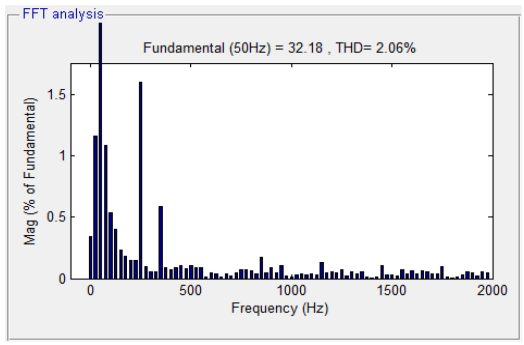

Fig. 14. Analysis of the harmonic spectrum of SHLRNN.

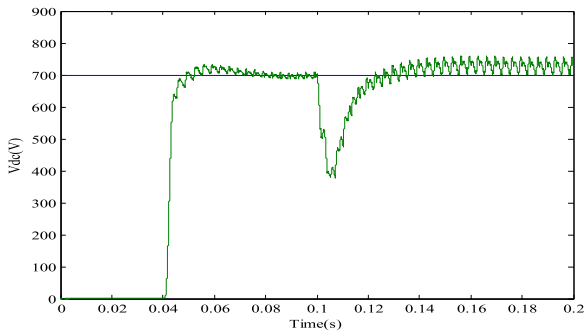

Fig. 15. DC-link voltage of the APF in the simulation.

dc-link voltage can converge to the reference value after a short time adjustment, demonstrating the robustness and stability of the designed approach on another aspect.

B. Compensation of Unbalanced Load Current

To evaluate the performance of the developed strategy, an unbalanced load is conducted on the APF via connecting a single-phase rectifier bridge between phase "1" and phase "2," followed by inductor $L = 10$ mH in series with a resistor $R = 40\ \Omega$. Fig. 16 plots the relevant curves. One could be realized that the source current is still compensated as stable sine wave rapidly even if the load current is unbalanced. Moreover, the THD under unbalanced load current is drawn in Fig. 17, which is quite low (1.60%). Regardless of the case of unbalanced load current, the system response is still in good condition, verifying the superior compensation capability for the unbalanced load current of the novel controller.

C. Compensation of Unbalanced Source Voltage

The simulation results under the condition of unbalanced source voltage are shown in Figs. 18 and 19. It can be seen that when the source voltage is unbalanced, the load current is also unbalanced, the output compensating current of APF can quickly track the unbalanced instruction current by utilizing the DHLFNN. Meanwhile the THD goes down to 1.56%, which means the designed method improves power quality and balances three-phase current. All the results have shown that the progressive approach makes the APF perform very well.

VI. Experimental Study

The experimental validation of the proposed control scheme for APF is tested experimentally on a single-phase prototype, which is shown in Figs. 20 and 21. Fig. 20 shows the overall diagram of the experimental device for the single-phase APF, and Fig. 21 shows the details of the prototype of the APF. The prototype is designed for a low rating because available equipment in the laboratory is rated at a lower value. Table II shows the nominal values of system parameters. The designed control algorithm is implemented on a dSPACE 1104 with a sampling frequency of 20 kHz. Test results are recorded by using Agilent DSO X3034A and power quality analysis module DSOX3PWR in the oscilloscope.

The Hall-effect voltage and current sensors are used with appropriate signal collection circuits for sensing source voltage, dc voltage, load current, and compensation current. Voltage boosting circuit is designed to convert PWM signal to meet the standards for the input voltage of IGBT driver.

Remark 1: Thanks to the proposed control strategy, the controller for each phase is independent. Although the novel controller is designed for three-phase APF, it is also suitable for single-phase APF with no need of redesign controller. Moreover, there is no three-phase power supply in our laboratory.

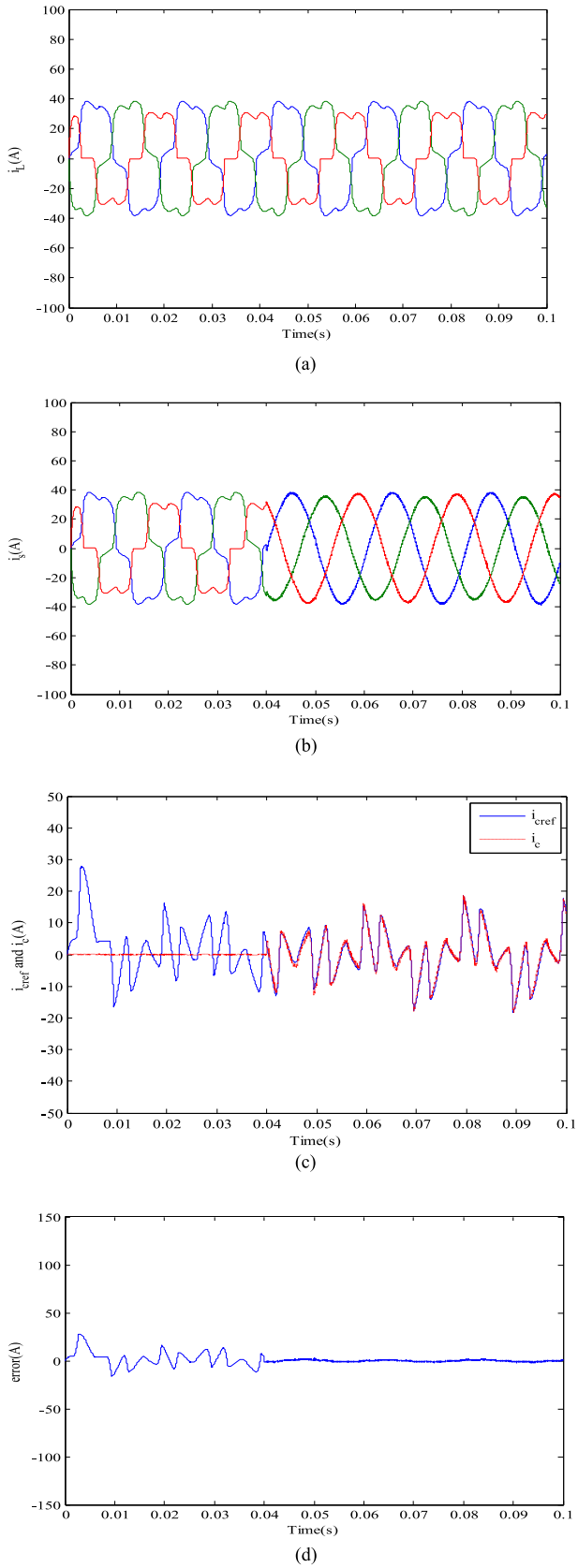

Fig. 16. System responses under the unbalanced load current. (a) Load currents of three phases. (b) Source currents of three phases. (c) The tracking trajectory of compensation current. (d) The tracking error of compensation current.

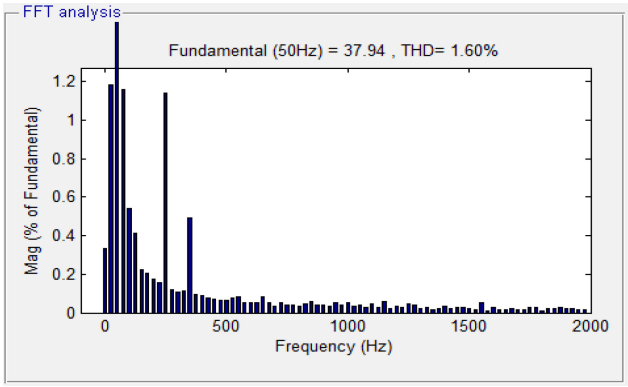

Fig. 17. Analysis of harmonic spectrum under unbalanced load current.

So a test platform for single-phase APF is built to validate the performances of the designed control algorithm.

A. Steady-State Experiment and Comparative Experiment

Figs. 22 and 23 show the system response and spectrum analysis in a steady state. The waveforms in Fig. 22 are the power supply voltage, load current, compensation current, and source current. It can be clearly seen that the source current is sinusoidal, proving the effect property of the control algorithm. Through spectrum analysis in Fig. 23, the total distortion rate of the source current is 30.57% before putting the APF into operation. While the THD is greatly reduced to 3.46% after making APF compensate the harmonic with the presented scheme. Furthermore, the source current and power supply voltage are in the same phase, achieving the purpose of compensating for harmonics and reactive current.

In order to verify the superiority of the proposed DHLFNN control strategy, the SHLFNN method is introduced to make comparisons. Fig. 24 shows the system response under the global sliding mode controller based on the SHLFNN. It can be seen from Fig. 25 that its THD is 5.23%, which is 1.77% higher than 3.46% under the control of the DHLFNN in Fig. 23(b), demonstrating the prior and satisfactory control effects of the proposed DHLFNN structure.

Fig. 26 draws the dc-link voltage of the APF in the experiment, from which it can be seen that when the loads change, the dc-link voltage can maintain stable value after a short time adjustment, demonstrating the robustness and stability of the designed approach on another aspect.

B. Dynamic Performance to Load Variations

To validate the dynamic response property of the proposed control scheme, it is advisable to take the following two cases into consideration: loads increase, i.e., 100%–150% load switching and loads decrease, i.e., 150% −100% load switching. Figs. 27 and 28 show the system response during sudden load increase and decrease, respectively. The waveforms in the figures are the source voltage, load current, compensation current, and source current. It is obvious that regardless of the sudden

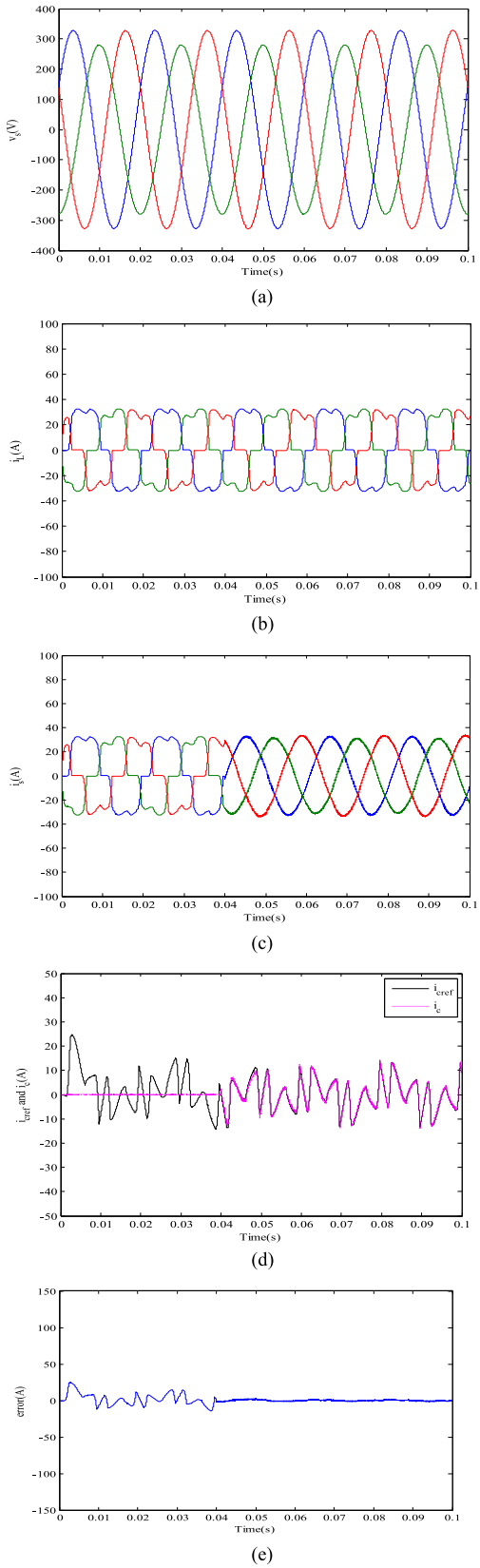

Fig. 18. System responses under unbalanced source voltage. (a) Unbalanced source voltage of three phases. (b) Load currents of three phases. (c) Source currents of three phases. (d) The tracking trajectory of compensation current. (e) The tracking error of compensation current.

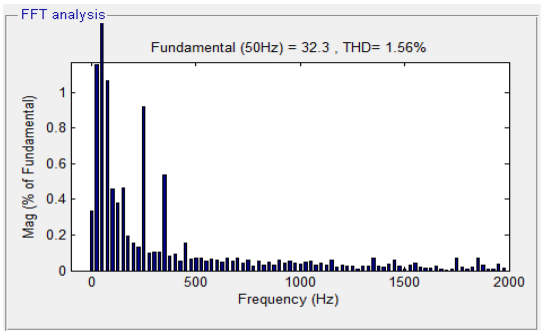

Fig. 19. Analysis of the harmonic spectrum under unbalanced source voltage.

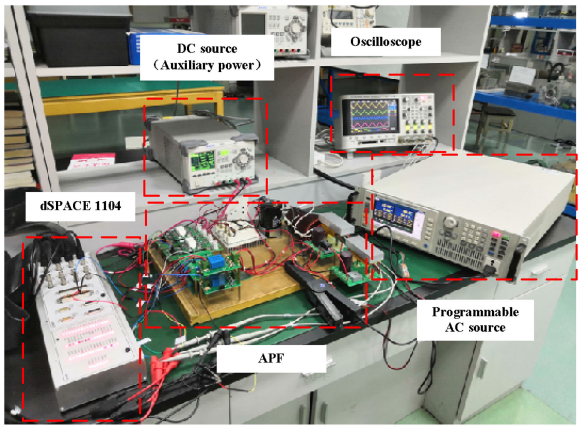

Fig. 20. Overall structure of the experimental prototype developed in the laboratory.

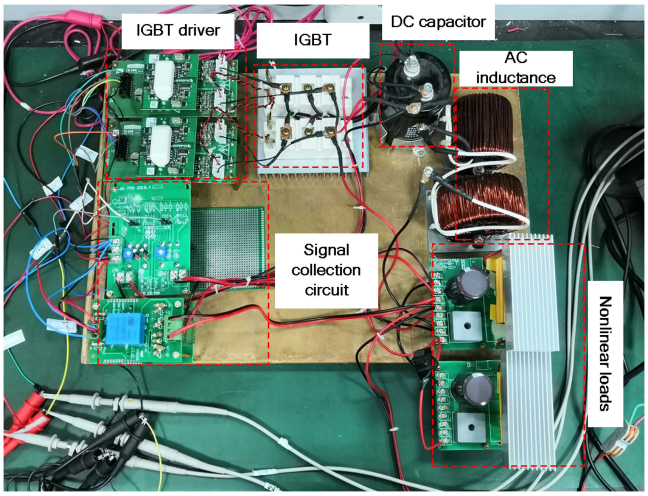

Fig. 21. Single-phase APF of the experimental prototype developed in the laboratory.

increase or sudden decrease of the loads, the source supply current can enter a new stable state after half a cycle by achieving a satisfactory dynamic effect. THDs of loads increase and loads decrease in Figs. 29 and 30; both of them are quite low under

TABLE II
SYSTEM PARAMETERS FOR EXPERIMENT

Supply voltage and frequency	$V_s = 24V, f = 50Hz$
Single-phase diode rectifiers parameters	$R = 15\Omega, C = 1mF$
Active power filter parameters	$L_c = 10mH$, $R_c = 0.1\Omega$, $C = 2200\mu F$, $v_{dcref} = 50V$
Switching frequency	$f_{sw} = 20KHz$

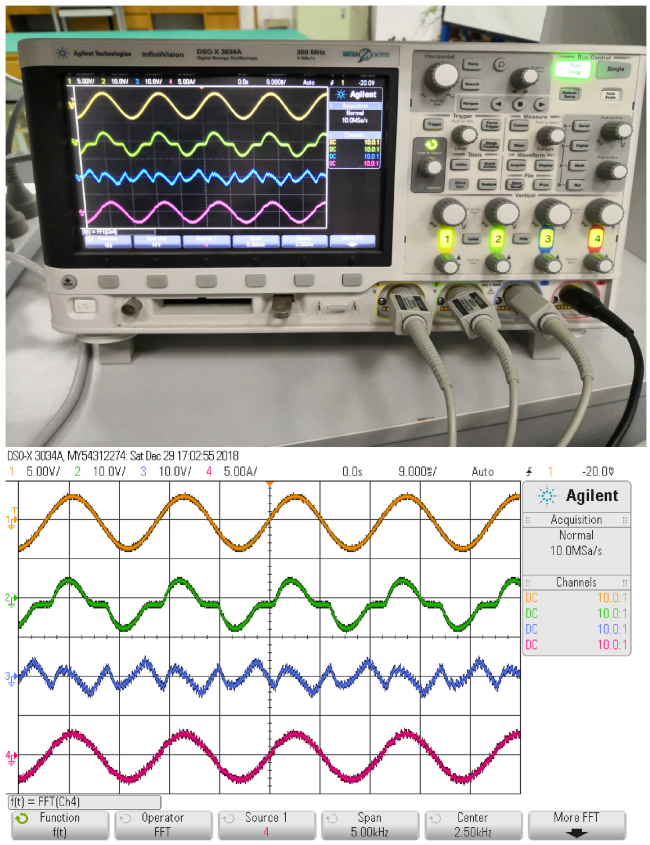

Fig. 22. Steady-state experimental results under DHLFNN, from top to bottom: source voltage, load current, compensation current, and source current.

the international standard, showing that the proposed controller has good robustness to the load variations.

C. APF Performances Under Abnormal Grid Voltage

The case of abnormal grid-voltage is considered for the APF to further evaluate the performance of the developed strategy. It contains two types of abnormal grid-voltage: voltage swell

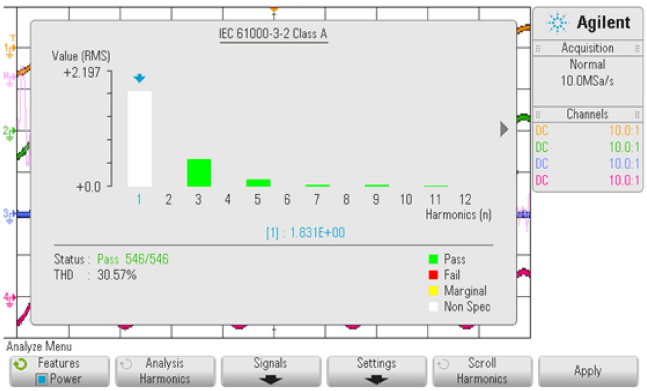

(a)

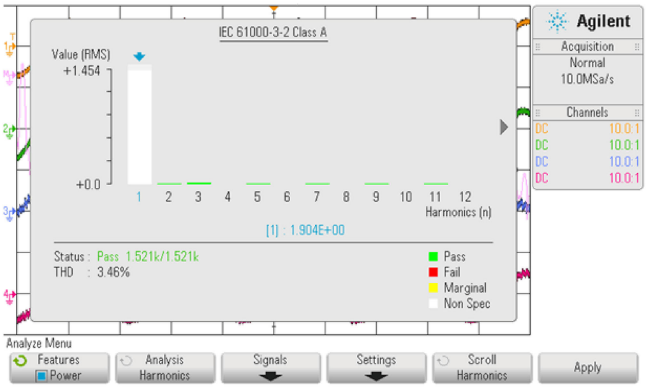

(b)

Fig. 23. Harmonic spectrum of source current under DHLFNN: (a) without APF and (b) with APF.

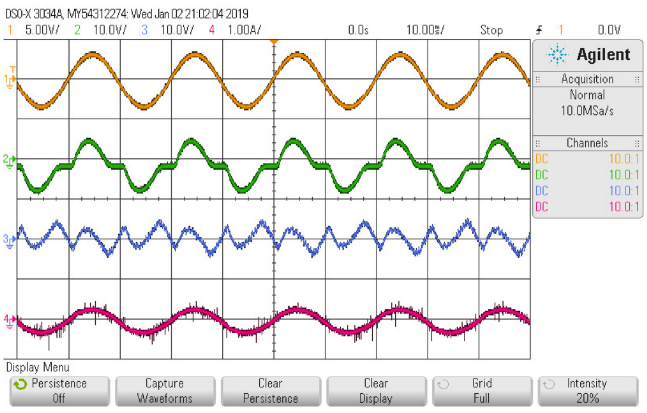

Fig. 24. Steady-state experimental results under SHLFNN, from top to bottom: source voltage, load current, compensation current, and source current.

and voltage sag. Figs. 31 and 32 depict the experimental responses under voltage swell and voltage sag. The waveforms in the plots are source voltage, load current, compensation current, and source current. It can be concluded that the APF system can obtain excellent compensation effect despite of the abnormal

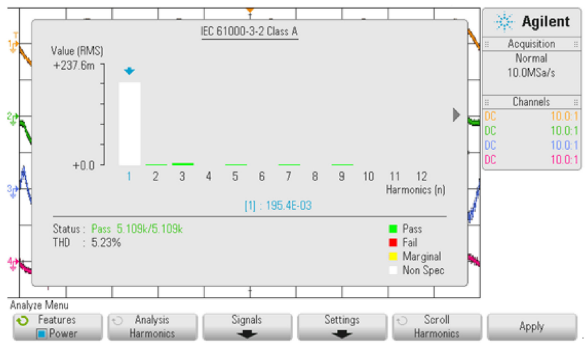

Fig. 25. Harmonic spectrum of source current under SHLFNN.

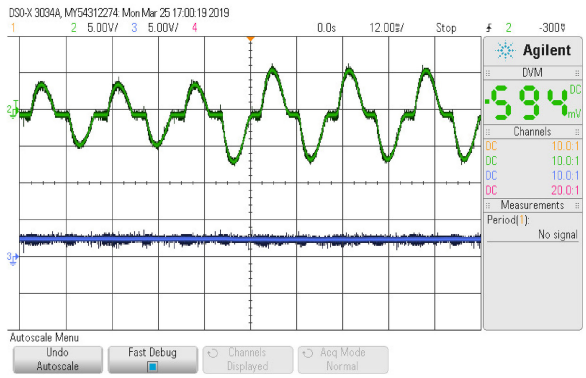

Fig. 26. DC-link voltage of the APF in the experiment, from top to bottom: load current and dc-link voltage.

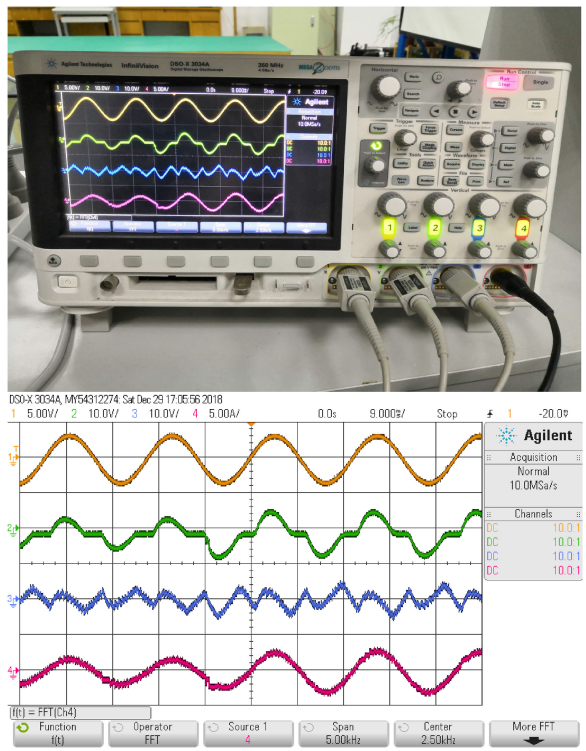

Fig. 27. Dynamic experimental results of loads increase, from top to bottom: source voltage, load current, compensation current, and source current.

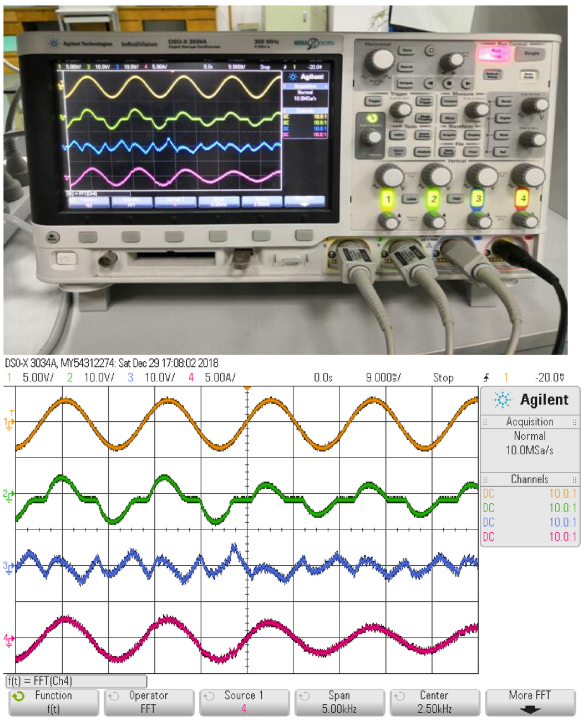

Fig. 28. Dynamic experimental results of loads decrease, from top to bottom: source voltage, load current, compensation current, and source current.

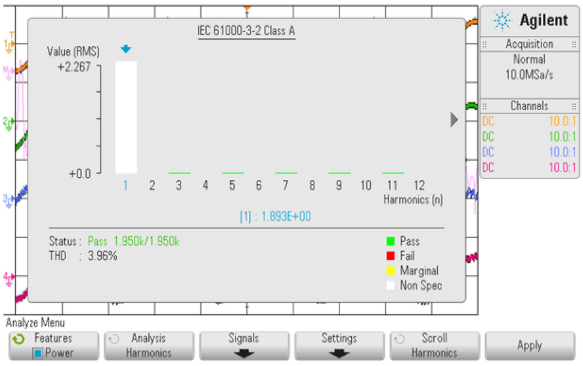

Fig. 29. Harmonic spectrum of loads increase.

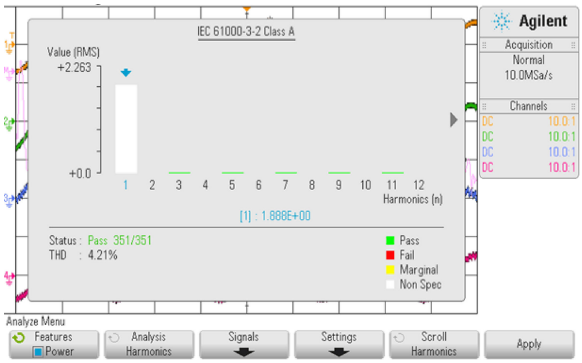

Fig. 30. Harmonic spectrum of loads decrease.

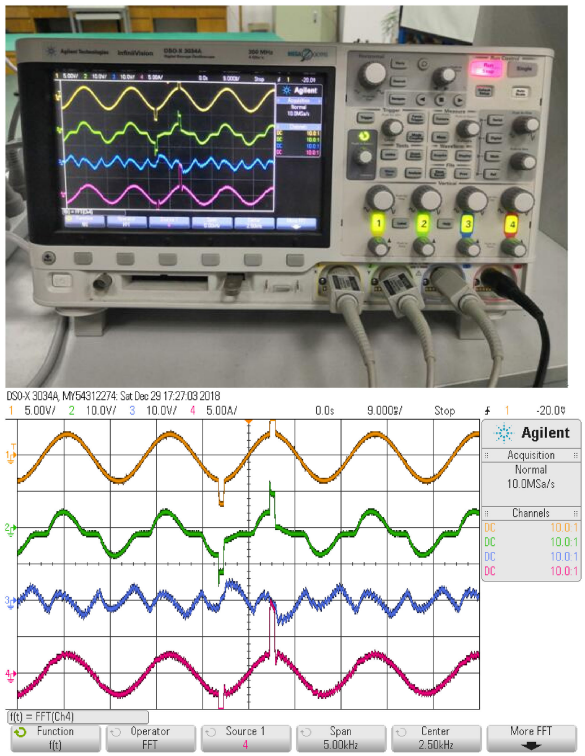

Fig. 31. Experimental results under voltage swell, from top to bottom: source voltage, load current, compensation current, and source current.

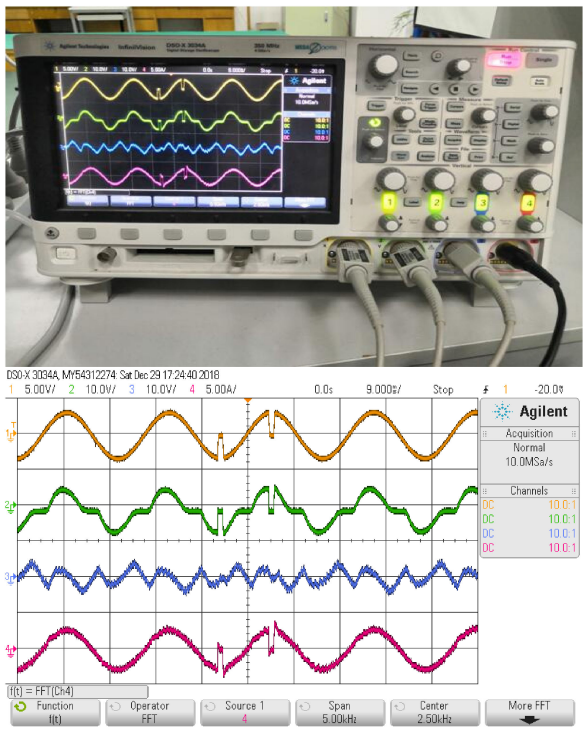

Fig. 32. Experimental results under voltage sag, from top to bottom: source voltage, load current, compensation current, and source current.

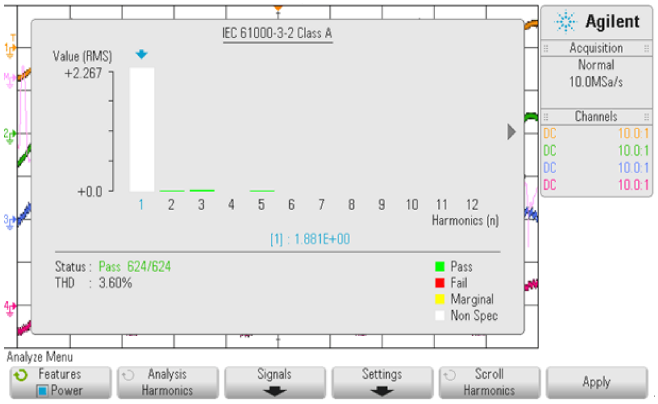

Fig. 33. Harmonic spectrum under voltage swell.

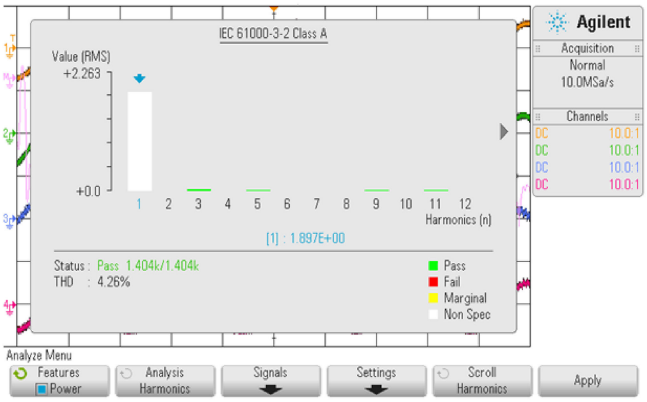

Fig. 34. Harmonic spectrum under voltage sag.

TABLE III
LIST OF ABBREVIATIONS

Full names	Abbreviations
Active power filter	APF
Neural network	NN
Double hidden layer output feedback neural network	DHLFNN
Single hidden layer output feedback neural network	SHLFNN
Global sliding mode control	GSMC
Proportional integral derivative	PID
Direct current	DC
Alternating current	AC
Total harmonic distortion	THD
Insulated gate bipolar transistor	IGBT
Pulse width modulation	PWM

grid voltage. At the same time, the analysis of harmonic spectrum in Figs. 33 and 34 also illustrates the stable property of the presented novel strategy.

VII. CONCLUSION

A proposed nonlinear control scheme of a DHLFNN compensator has been established, simulated, and implemented by using the DS1104 digital real-time controller board of dSPACE. On one hand, the deep network of double hidden layer neural has the merits of high precision, fast speed, strong generalization ability, and efficient training regardless of requiring few neurons. On the other hand, output FNN that has output feedback loops can better approach the unknown function by storing more network information. Not only the simulation studies suggest the wonderful control effect of the proposed original algorithm, but also the hardware experimental results demonstrate the perfect harmonic compensation capability. Besides, comparisons with other advanced control method are made to further verify the superior and satisfactory system performance of the novel approach. Eventually, the simulation and experimental results demonstrate that the proposed method is quite satisfactory to mitigate harmonic distortions and reactive power compensation from different aspects.

ACKNOWLEDGMENT

The authors would like to thank the anonymous reviewers for their useful comments that improved the quality of this paper.

REFERENCES

[1] W. Tareen and S. Mekhielf, "Three-phase transformerless shunt active power filter with reduced switch count for harmonic compensation in grid-connected applications," *IEEE Trans. Power Electron.*, vol. 33, no. 6, pp. 4868–4881, Jun. 2018.
[2] S. Swain, P. Ray, and K. Mohanty, "Improvement of power quality using a robust hybrid series active power filter," *IEEE Trans. Power Electron.*, vol. 32, no. 5, pp. 3490–3498, May 2017.
[3] X. Du, L. Zhou, H. Lu, and H. Tai, "DC link active power filter for three-phase diode rectifier," *IEEE Trans. Ind. Electron.*, vol. 59, no. 3, pp. 1430–1442, Mar. 2012.
[4] A. Javadi, A. Hamadi, L. Woodward, and K. Al-Haddad, "Experimental investigation on a hybrid series active power compensator to improve power quality of typical households," *IEEE Trans. Ind. Electron.*, vol. 63, no. 8, pp. 4849–4859, Aug. 2016.
[5] Z. Luo, M. Su, Y. Sun, W. Zhang, and Z. Lin, "Analysis and control of a reduced switch hybrid active power filter," *IET Power Electron.*, vol. 9, pp. 1416–1425, 2016.
[6] M. Angulo, D. Ruiz-Caballero, J. Lago, M. Heldwein, and S. Mussa, "Active power filter control strategy with implicit closed- loop current control and resonant controller," *IEEE Trans. Ind. Electron.*, vol. 60, no. 7, pp. 2721–2730, Jul. 2013.
[7] C. Lam, L. Wang, S. Ho, and M. Wong, "Adaptive thyristor-controlled LC-hybrid active power filter for reactive power and current harmonics compensation with switching loss reduction," *IEEE Trans. Power Electron.*, vol. 32, no. 10, pp. 7577–7590, Oct. 2017.
[8] A. Bhattacharya, C. Chakraborty, and S. Bhattacharya, "Parallel-connected shunt hybrid active power filters operating at different switching frequencies for improved performance," *IEEE Trans. Ind. Electron.*, vol. 59, no. 11, pp. 4007–4019, Nov. 2012.
[9] T. Lee and S. Hu, "Discrete frequency-tuning active filter to suppress harmonic resonances of closed-loop distribution power systems," *IEEE Trans. Power Electron.*, vol. 26, no. 1, pp. 137–148, Jan. 2011.

[10] S. Rahmani, A. Hamadi, K. Al-Haddad, and L. Dessaint, "A combination of shunt hybrid power filter and thyristor-controlled reactor for power quality," *IEEE Trans. Ind. Electron.*, vol. 61, no. 5, pp. 2152–2164, May 2014.
[11] A. Ray and A. Bhattacharya, "Improved tracking of shunt active power filter by sliding mode control," *Int. J. Elect. Power*, no. 78, pp. 916–925, Jun. 2016.
[12] S. Hou, J. Fei, C. Chen, and Y. Chu, "Finite-time adaptive fuzzy-neural-network control of active power filter," *IEEE Trans. Power Electron.*, vol. 34, no. 10, pp. 10298–10313, Oct. 2019.
[13] R. Ribeiro, C. Azevedo, and R. Sousa, "A robust adaptive control strategy of active power filters for power-factor correction, harmonic compensation, and balancing of nonlinear loads," *IEEE Trans. Power Electron.*, vol. 27, no. 2, pp. 718–730, Feb. 2012.
[14] J. Diarmaid, J. Francisco, G. John, and L. Gordon, "An adaptive digital control scheme for improved active power filtering under distorted grid conditions," *IEEE Trans. Ind. Electron.*, vol. 65, no. 2, pp. 988–999, Feb. 2018.
[15] Z. Zou, K. Zhou, Z. Wang, and M. Cheng, "Frequency-adaptive fractional-order repetitive control of shunt active power filters," *IEEE Trans. Ind. Electron.*, vol. 62, no. 3, pp. 1659–1668, Mar. 2015.
[16] S. Hou and J. Fei, "Adaptive fuzzy backstepping control of three-phase active power filter," *Control Eng. Pract.*, vol. 45, pp. 12–21, Dec. 2015.
[17] M. Pai, "Quasi-output feedback global sliding mode tracker for uncertain systems with input nonlinearity," *Nonlinear Dyn.*, vol. 86, no. 2, pp. 1215–1225, Oct. 2016.
[18] G. Aurelio, P. Omar, F. Vicente, R. Pedro, and G. Pablo, "Application of a repetitive controller for a three-phase active power filter," *IEEE Trans. Ind. Electron.*, vol. 22, no. 1, pp. 237–246, Jan. 2007.
[19] L. Saribulut, A. Teke, and M. Tümay, "Artificial neural network-based discrete-fuzzy logic controlled active power filter," *IET Power Electron.*, vol. 7, no. 6, pp. 1536–1546, Jun. 2014.
[20] Y. Chu, J. Fei, and S. Hou, "Dynamic global proportional integral derivative sliding mode control using radial basis function neural compensator for three-phase active power filter," *Trans. Inst. Meas. Control*, vol. 40, no. 12, pp. 3549–3559, Aug. 2018.
[21] Z. Hu, W. Hu, and Z. Wang, "Global sliding mode control based on a hyperbolic tangent function for matrix rectifier," *J. Power Electron.*, vol. 17, no. 4, pp. 991–1003, Jul. 2017.
[22] D. Efimov and L. Fridman, "Global sliding-mode observer with adjusted gains for locally Lipschitz systems," *Automatica*, vol. 47, no. 3, pp. 565–570, Mar. 2011.
[23] S. Mobayen and D. Baleanu, "Linear matrix inequalities design approach for robust stabilization of uncertain nonlinear systems with perturbation based on optimally-tuned global sliding mode control," *J. Vib. Control*, vol. 23, no. 8, pp. 1285–1295, May 2017.
[24] Q. Yang, S. Jagannathan, and Y. Sun, "Robust integral of neural network and error sign control of MIMO nonlinear systems," *IEEE Trans. Neural Netw. Learn. Syst.*, vol. 26, no. 12, pp. 3278–3286, Dec. 2015.
[25] Y. Liu, J. Li, S. Tong, and C. Chen, "Neural network control-based adaptive learning design for nonlinear systems with full-state constraints," *IEEE Trans. Neural Netw. Learn. Syst.*, vol. 27, no. 7, pp. 1562–1571, Jul. 2016.
[26] J. Fei and C. Lu, "Adaptive fractional order sliding mode controller with neural estimator," *J. Franklin Inst.*, vol. 355, no. 5, pp. 2369–2391, Mar. 2018.
[27] K. Bouhoune, K. Yazid, M. Boucherit, and A. Cheriti, "Hybrid control of the three phase induction machine using artificial neural networks and fuzzy logic," *Appl. Soft Comput.*, vol. 55, pp. 289–301, Jun. 2017.
[28] X. Fu and S. Li, "Control of single-phase grid-connected converters with *LCL* filters using output feedback neural network and conventional control methods," *IEEE Trans. Power Electron.*, vol. 31, no. 7, pp. 5354–5364, Oct. 2015.
[29] S. Li, H. Wang, and M. Rafique, "A novel output feedback neural network for manipulator control with improved noise tolerance," *IEEE Trans. Neural Netw. Learn. Syst.*, vol. 29, no. 5, pp. 1908–1918, Apr. 2017.
[30] J. Fei and C. Lu, "Adaptive sliding mode control of dynamic systems using double loop output feedback neural network structure," *IEEE Trans. Neural Netw. Learn. Syst.*, vol. 29, no. 4, pp. 1275–1286, Apr. 2018.
[31] J. Wiest and G. Buckner, "Indirect intelligent sliding mode control of antagonistic shape memory alloy actuators using hysteretic output feedback neural networks," *IEEE Trans. Control Syst. Technol.*, vol. 22, no. 3, pp. 921–929, Jul. 2013.
[32] F. El-Sousy, "Adaptive dynamic sliding-mode control system using output feedback RBFN for high-performance induction motor servo drive," *IEEE Trans. Ind. Inform.*, vol. 9, no. 4, pp. 1922–1936, Jan. 2013.
[33] L. Bachtiar, C. Unsworth, and R. Newcomb, "Super E-Noses: Multi-layer perceptron classification of volatile odorants from the firing rates of cross-species olfactory receptor arrays," in *Proc. 36th Annu. Int. Conf. Eng. Med. Biol. Soc.*, Chicago, IL, USA, Aug. 26–30, 2014, pp. 954–957.
[34] N. Ahmadi and G. Akbarizadeh, "Hybrid robust iris recognition approach using iris image pre-processing, two-dimensional gabor features and multi-layer perceptron neural network/PSO View Document," *IET Biometrics,* vol. 7, no. 2, pp. 153–162, Mar. 2018.
[35] W. Makondo *et al.*, "Exploratory test oracle using multi-layer perceptron neural network," in *Proc. Int. Conf. Adv. Comput., Commun. Inform.*, Jaipur, India, Sep. 21–24, 2016, pp. 1166–1171.
[36] J. Esmaily, R. Moradinezhad, and J. Ghasemi, "Intrusion detection system based on multi-layer perceptron neural networks and decision tree," in *Proc. 7th Conf. Inf. Knowl. Technol.*, Urmia, Iran, May 26–28, 2015, pp. 1–5.

Juntao Fei (M'03–SM'14) received the B.S. degree in electrical engineering from Hefei University of Technology, Hefei, China, in 1991, the M.S. degree in electrical engineering from the University of Science and Technology of China, Hefei, in 1998, and the M.S. and Ph.D. degrees in mechanical engineering from The University of Akron, Akron, OH, USA, in 2003 and 2007, respectively.

From 2002 to 2003, he was a Visiting Scholar with the University of Virginia, Charlottesville, VA, USA. From 2007 to 2009, he was a Postdoctoral Research Fellow and Assistant Professor with the University of Louisiana, Lafayette, LA, USA. He is currently a Professor with Hohai University, Nanjing, China. His research interests include adaptive control, nonlinear control, intelligent control, dynamics and control of MEMS, and smart materials and structures.

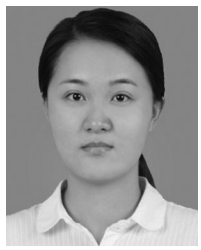

Yundi Chu received the B.S. and M.S. degrees in electrical engineering, in 2013 and 2016, respectively, from Hohai University, Nanjing, China, where she is currently working toward the Ph.D. degree in electrical engineering.

Her research interests include power electronics, adaptive control, intelligent control, and nonlinear control.